Acta Materialia 149 (2018) 206–219

Contents lists available at ScienceDirect

Acta Materialia

journal homepage: www.elsevier.com/locate/actamat

Full length article

Loop and void damage during heavy ion irradiation on nanocrystalline and coarse grained tungsten: Microstructure, effect of dpa rate, temperature, and grain size

O. El-Atwani [a, *], E. Esquivel [a], M. Efe [b], E. Aydogan [a], Y.Q. Wang [a, c], E. Martinez [a], S.A. Maloy [a]

[a] Materials Science and Technology Division, Los Alamos National Laboratory, Los Alamos, NM, USA
[b] Metallurgical and Materials Engineering, Middle East Technical University, Ankara, Turkey
[c] Center for Integrated Nanotechnology, Los Alamos National Laboratory, Los Alamos, NM, USA

ARTICLE INFO

Article history:
Received 8 September 2017
Received in revised form
31 January 2018
Accepted 13 February 2018
Available online 20 February 2018

Keywords:
Heavy ion irradiation
Grain size
Electron microscopy
Voids
Dislocation loops
Burgers vector

ABSTRACT

Displacement damage, through heavy ion irradiation was studied on two tungsten grades (coarse grained tungsten (CGW) and nanocrystalline and ultrafine grained tungsten (NCW)) using different displacement per atom rates and different irradiation temperatures (RT and 1050 K). Percentage of <111> and <100> type loops at the irradiation conditions was determined. Irradiation damage in the microstructure was quantified using average loop areas and densities (method A) and loop areal fraction in the grain matrices under 2-beam diffraction conditions (method B). Average values of <111> and <100> loops were calculated from method A. Loop coalescence was shown to occur for CGW at 0.25 dpa. Using both methods of quantifying microstructural damage, no effect of dpa rate was observed and damage in CGW was shown to be the same at RT and 1050 K. Swelling from voids observed at 1050 K was quantified. The loop damage in NCW was compared to CGW at the same diffraction and imaging conditions. NCW was shown to possess enhanced irradiation resistance at RT regarding loop damage and higher swelling resistance at 1050 K compared to CGW. For irradiation at 1050 K, the NCW was shown to have similar defect densities to the CGW which is attributed to higher surface effects in the CGW, vacancy loop growth to voids and a better sink efficiency in the CGW deduced from the vacancy distribution profiles from Kinetic Monte Carlo simulations. Loop density and swelling was shown to have similar values in grains sizes that range from 80 to 600 nm. No loop or void denuded zones occurred at any of the irradiation conditions. This work has a collection of experiments and conclusions that are of vital importance to materials and nuclear energy communities.

Published by Elsevier Ltd on behalf of Acta Materialia Inc.

1. Introduction

Tungsten is considered to be the primary choice as a plasma material interface (PMI) in fusion reactors [1]. For these applications, tungsten will be exposed to high doses of low energy helium ($10-10^4$ eV) and 14.1 MeV neutron irradiation of approximately hundreds of dpa for an anticipated 3–5 year lifetime [2,3] which leads to irradiation damage denoted by the formation of interstitial loops, dislocations, vacancy clusters, helium bubbles [4,5], and cavities [6–10]. The irradiation damage alters the thermal [11,12] and mechanical properties [13,14] of the material and changes its microstructure [15–17]. The degradation of the mechanical properties can lead to serious issues such as failure of the components [13]. Such degradation is manifested by the embrittlement and hardening of the material, creep, and changes in the ductile to brittle transition temperature [18,19]. These challenges prompted the investigation of other alternative materials such as tungsten alloys and ultrafine (UF) and nanocrystalline (NC) tungsten (refined grained tungsten) [20,21].

NC materials are considered to be highly radiation tolerant due to their high density of grain boundaries which, in turn, act as defect (i.e. irradiation induced defects) [10,22–24] and particle (e.g. the helium ash from the deuterium-tritium reaction in fusion reactors) [25] sinks and enhance defect annihilation [26]. This is

* Corresponding author.
E-mail address: oelatwan25@gmail.com (O. El-Atwani).

https://doi.org/10.1016/j.actamat.2018.02.035
1359-6454/Published by Elsevier Ltd on behalf of Acta Materialia Inc.

believed to lead to a high dose threshold for the aforementioned undesired changes in the material matrix. The enhanced irradiation tolerance performance of nanocrystalline materials was illustrated on several BCC and FCC metallic materials as well as ceramic materials [6,27–35].

Recently, studies regarding helium irradiation on NC tungsten and other BCC materials demonstrated a logarithmic trend of bubble density and swelling as a function of grain size over a temperature threshold [32,33,36]. Heavy ion irradiation on tungsten at RT demonstrated a surprising trend of defect density decrease as the grain size increased in the ultrafine (100–500 nm) regime. This was demonstrated to be a result of defect coalescence in the large grains [37]. Different NC materials, however, showed a variation in their response to irradiation damage. Their response depends on the irradiation conditions, synergistic effects, and their sink efficiency (grain boundary character) type which is usually experimentally characterized by the width of denuded zones (loop-free zones near the grain boundaries) [38].

Heavy ion irradiation is used to simulate neutron irradiation in materials [39–42]. However, the dpa rate during ion irradiations is orders of magnitude higher than the dpa rate during neutron irradiation [43] and therefore, heavy ion irradiations have to be performed at higher temperatures to introduce similar defect density and size distributions [44]. Recently, Dunn et al. [44] performed spatially resolved stochastic cluster dynamics (SRSCD) to study the temperature shift required during heavy ion irradiation to simulate neutron irradiation damage. Their results showed that a temperature shift of 100–200 °C is needed to correlate heavy ion irradiation with neutron irradiation results on BCC Fe.

Several studies have used different heavy ions to investigate the early stage neutron damage on tungsten [8–10,45–48]. Defect configurations, geometries and distributions were studied by Yi et al. [8,9]. Effect of the heavy ion type, the damage stages and grain size effect in the ultrafine regime were examined by El-Atwani et al. [10]. Synergistic effect with He ions were also studied by Zhang et al. [48]. However, there are still several outstanding questions that need to be answered regarding irradiation damage in tungsten. The first outstanding question is the Burgers vector type of the loops formed during heavy ion irradiation. Sand et al. [49] analyzed MD simulations for 150 keV collision cascades on W. In D-D potential simulations, small loops (with 35–80 self-interstitials, SIAs) were shown to be 50% <111> Burgers vector and fifty percent <100> Burgers vector, while in A-T potential simulations only one <100> type loop was predicted. No vacancy loops were found using D-D potential while one vacancy loop formed from the cascade collapse with the A-T potential. Setyawan et al. [50], via MD simulations, predicted the formation of rare <100>{110}SIA loops at 1025 K (similar to the high temperature in this study) but not at 300 K (similar to the room temperature in this study). However, vacancy loops of <100>{100} or cavities were shown to occur at both 300 K and 1025 K. Such loops were shown to form directly in the higher energy cascade. Others [51–53] used 30–60 keV Au^+ to irradiated tungsten foils at RT and have found vacancy type <111>{110} loops and few pure edge <110> loops which are explained to form from cascade vacancy core collapse. Yi et al. [9] demonstrated that all loops at 1075 K are of <111> type (using 150 keV self-ion irradiation). At higher energies (2 MeV), Yi et al. [8] found the percentage of <100> loops to be approximately 10 at 1023 K. The authors argue that these <100> loops are not stable at high temperatures. Yi et al. used weak beam dark field imaging and loops of less than 4 nm were disregarded. The second outstanding question is the effect of grain size (direct comparison between nanocrystalline or ultrafine grained tungsten with coarse grained tungsten), dpa rata and temperature on the irradiation damage and the methods in which a total irradiation damage can be quantified. The third outstanding question is the mechanism of loop rafting (a phenomenon which is observed in heavy ion and neutron irradiated BCC metals) [9,43,48,54,55]. Lastly, the fourth outstanding question is void formation under heavy ion or neutron irradiation and the stability of these voids as a function of dpa. Evans et al. [56] who showed a decrease in void sizes on neutron irradiated molybdenum as a function of dpa. The shrinkage of the voids was shown to occur due to the change in the rate of vacancy jumps to voids. This can occur when vacancy loops start to grow at the sites of the voids. The voids will add another interstitial biased microstructure (in addition to dislocation networks) thus absorbing interstitials and giving rise to net absorption of vacancies to the vacancy loops. Swelling will probably decrease as a function of dpa.

This work attempts to answer these outstanding questions by performing heavy ion (Cu^+) irradiation on W thin foils. We first determine the Burgers vector of the loops via bright field transmission electron microscopy (TEM) images at different two beam conditions on all visible loops. Second, we perform two different methods to quantify irradiation damage (taking into account both loop density and sizes) and compare the damage for two dpa rates (using two dpa rates of 100 magnitude difference), and two different extreme temperatures (RT and 1050 K). The performance of nanocrystalline and ultrafine tungsten is also compared with coarse grained tungsten at low dpa rates. Kinetic Monte Carlo (KMC) simulations are performed to plot the steady state vacancy profile across an interface and discuss the sink efficiency vs. grain boundary density effects on the performance of nanocrystalline- and coarse-grained tungsten. Third, we summarize detailed TEM results (details are presented elsewhere) on the discovery of the rafting mechanism. Finally, void swelling and void shrinkage is studied.

2. Experimental

2.1. Samples

Two tungsten sample grades were used in this study. The first grade is a nanocrystalline and ultrafine tungsten (NCW) grade produced by an orthogonal machining process. The details of this process were mentioned elsewhere [20]. Both nanocrystalline (< 100 nm) and ultrafine (100–500 nm) [57,58] grains coexist in this grade. The second tungsten grade is a coarse grained tungsten (CGW with grains that are larger than 1 μm) provided by ESPI metals, USA. Both grades are high purity (nominally 99.95 and 99.99% for the NCW and the CGW respectively).

TEM samples were prepared from both grades via electropolishing with 0.5% NaOH solution. The average samples thickness is ~100 nm. The grain morphology and texture of the samples prior to irradiation are shown in Fig. 1. Both grades have a high fraction of low angle grain boundaries (LAGBs) (~50% and 65% for the CGW and NCW grades respectively).

2.2. Irradiation

Irradiation of the thin foil samples was performed in the Ion Beam Materials Laboratory (IBML) at Los Alamos National Laboratory (LANL). Irradiation was performed using the Tandem accelerator with 3 MeV Cu^+ ions at normal incidence. The irradiation was performed *ex-situ* using two different displacement per atom (dpa) rates (0.0167 and 0.000167 dpa/s) at two different temperatures (RT and 1050 K). The samples were irradiated to different dpa values ranging from 0.2 to 4 dpa. To determine the dpa and the dpa rate, the Kinchin-Pease model in the Stopping Range of Ions in Matter (SRIM) Monte Carlo computer code (version 2013) [59] was used to determine the damage event (which was 0.76 vacancy/Ion/

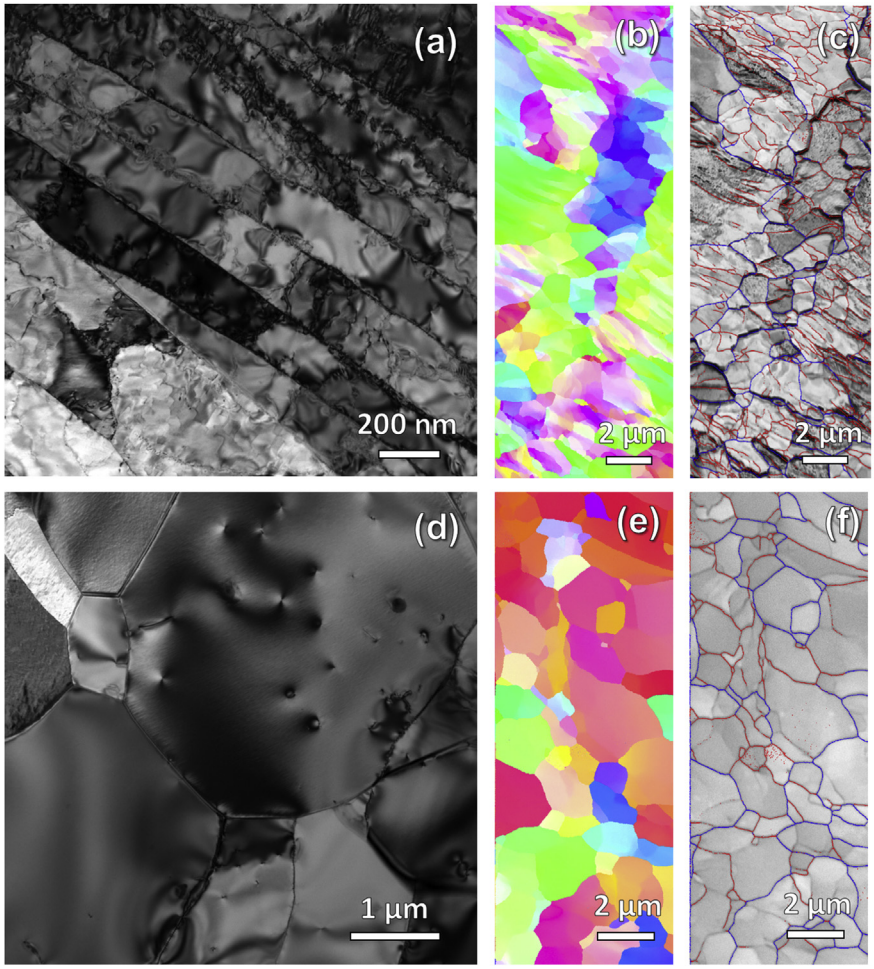

Fig. 1. (a), (d) Bright-field TEM images (b), (e) EBSD inverse pole-figure (IPF) orientation maps (c), (f) and grain boundary angle maps of NCW and CGW respectively prior to irradiation. Red color denotes LAGBs (orientation 2–15°) and black color denotes HAGBs (orientation angle of 15–180°). Only data with confidence index of over 0.5 was taken. (For interpretation of legend colors, the reader is directed to the online version). Figure 1b shows a textured sample (LAGBs are not very clear). For the NCW grain size interpretation, the reader is directed to Figure 1a and c.

Å) in 100 nm sample thickness using 40 eV as a displacement damage threshold in tungsten [60].

2.3. Characterization and quantification

Samples before and after irradiations were characterized via transmission electron microscopy (TEM) using an FEI-Tecnai-G2-F30 transmission electron microscope with electron beam energies of 300 keV in the Electron Microscopy Laboratory (EML) at LANL. Texture of the samples prior to irradiation was determined via electron backscattered diffraction (EBSD) method performed in an FEI Inspect FEG SEM equipped with TSL EBSD detector using an acceleration voltage of 20 kV. EBSD was performed on the electropolished TEM samples. Imaging of voids was performed using Fresnel conditions (voids appear bright with under-focused electron beam and dark with over-focused electron beam). Processing of images was performed using Image J software. In a typical TEM image, some dislocation loops are invisible at g.b = 0 (invisibility criteria) where g is the diffraction vector and b is the burgers vector of the loop [5]. Therefore, to minimize quantification error in measuring the total defect density, multi-beam imaging conditions was used [4]. Quantification error can also occur due to image forces, glissile prismatic loop glide to the surface, and foil thickness changes [4]. Grains used in quantification were taken from closed regions in the sample of ~100 nm thickness The above factors affect the absolute values but not the trends and therefore, in this work, trends will be compared.

Determination of the loop burgers vectors and the percentages was performed using two-beam bright field TEM conditions near the [001] zone axis (both [110] and [200] g vectors were used) following the work by Yi et al. [8]. The invisibility criteria (g.b = 0) was used. Loop image sizes at the irradiation conditions mentioned in the paper are measured using the same zone axis imaging and the g vector of [200] since loop contrasts are proportional to g.b. For loop and void counting, circles were drawn in every image and the number of loops in every circle was counted before taking the average. A similar procedure is detailed elsewhere with an explanation of the error bar determination [33,37]. Sizes were found in a similar manner.

2.4. Kinetic Monte Carlo (KMC) simulations

KMC [61–66] simulations of the evolution of damage at both RT and 1050 K were performed to study the steady state vacancy profile. The energy barriers used in the KMC for vacancies and self-interstitials were 1.667 and 0.057 eV, respectively. An interface has been model as a region in space where a larger barrier for defects to escape exists, given by the binding energy. 1 eV binding energy for vacancies and 1.5 eV for interstitials to the interface has been assumed. The migration energy of self-interstitials at the interface

itself was set to 0.557 eV while for the vacancies the barrier was equal as in bulk. The dose rate was 10^{-4} dpa/s and the grain size is about 50.6 nm.

3. Results and discussion

3.1. Burgers vector of loops in irradiated samples

To determine the Burgers vector of loops in the irradiated samples, 2-beam g.b analysis was performed using the g <200> and <110> vectors near the [001] zone axis and (Fig. 2). Upon tilting between the two g vectors, loops of two Burgers vector types were observed. The Burgers vector of the loops in irradiated tungsten was shown to be of <111> and <100> type. Therefore, seven possibilities exist. Following the procedure by Yabuuchi et al. [67] and Yi et al. [8], using the <200> g vector, the four variants of the <111> and one variant of the <100> Burgers vectors will be present and using the <110> g vector, two variants of each will be present. Therefore, a set of two equations can be solved to determine the Burgers vector of loops in the irradiated samples. This analysis was performed on the CGW at 0.25 dpa where 1–2 μm grains are present to allow tilting in the microscope. The analysis was performed in samples irradiated in four different conditions (RT and 1050 K for the dpa rates). Fig. 3 shows the Burgers vector percentage in the four different conditions. An increase in the percentage of <111> loops was observed at 1050 K using the low dpa rate. For the high dpa rate, the opposite occurred. This is inconsistent with the work by Yi et al. [8,9]. We attribute the discrepancy to the differences in sizes of loops that were analyzed. In the weak beam dark field analysis of Yi et al., they neglected analyzing loops of sizes below 4 nm. The summary of our findings regarding the loop type is compared with other research in literature in Table 1.

<100> loops were demonstrated to form in BCC irradiated metals. In the BCC iron (Fe) system, loops with <100> Burgers vectors, thought to be unique in BCC metals, are more prevalent at high temperatures. A transition temperature was shown to exist for the transition from <111> loop dominated microstructure to a <100> dominated one [68–70]. Such a transition was shown to occur due to the relative mobilities of the <111> and <100> loops (where <111> loops can migrate to free surfaces or sinks unlike the sessile <100> loop) [70] and stabilities (instabilities of magnetic spins) [71]. The formation of <100> loops, however, was explained via different mechanisms. They can form either directly from the cascade [72], or interaction of two <111> loop variants [73,74] or the spontaneous switch of the Burgers vector [75]. They were also shown to form through the Eyre-Bullough mechanism [76]. This mechanism states that loops can nucleate to form <110> Burgers vector loops with an enclosed stacking fault which can then shear to {100} and {110} directions to produce loops of Burgers vectors of <100> and <111> type respectively. A modified version of this mechanism was suggested by Marian and Wirth (via Molecular Dynamics Simulations, MD) in which <111> Burgers vector loops of the same size interact with one another in steps to form <100> loops [73]. The recent modeling work by Setyawan et al. [50] which demonstrated <100> vacancy type of loops of tungsten at both RT and 1050 K (similar to this work) gave insight on the need to more studies on heavy ion irradiated tungsten to understand the loop structure and behavior. We have performed some analysis of loop types and the corresponding sizes and we show that most of the small loops are of <100> type as will be discussed later. .

3.2. Loop density and total microstructural damage

The loop density was determined for every irradiation condition in this work. To determine the loop density, we performed TEM imaging at high magnifications using multibeam imaging condition to capture the seven possible Burgers vectors (<111> and <100> variants).

Fig. 4 shows a comparison between the CGW and NCW at 1 dpa, 0.000167 dpa/s, at either RT or 1050 K. At both temperatures, the loop density of the CGW seems to be lower than the NCW. Based on the grain boundary density of the two samples, more efficient absorption of defects is expected to occur in the NCW. Loop density measurements can be misleading when it pertains to the quantification of irradiation damage. Loops, depending on their size or irradiation conditions (eg. temperature), can show coalescence. Recently, El-Atwani et al. [37] demonstrated loop coalescence on irradiated nanocrystalline and ultrafine Fe via measurements of the loop density and loop area of the same grains at similar diffraction conditions but at different doses. A decrease in loop density with increasing dose, indicative of coalescence, was observed in ultrafine grains. Fig. 5 shows the loop density measurement vs. grain size in the NCW as a function of dpa. Loop density increased with dpa up to 2 dpa. Loop density remained similar between 2 dpa and 3 dpa. Above 3 dpa, the loop density decreased for all grain sizes. This indicates loop coalescence on the small grains after 2 dpa in the NCW. At 4 dpa, the loop density of larger grains in the ultrafine regime (> 200 nm) decreased, suggestive of significant loop coalescence in the larger grained samples.

Therefore, with the occurrence of loop coalescence, irradiation damage quantification using loop densities only is inaccurate. In order to compare the irradiation damage vs temperature, grain size (NCW vs CGW) and dpa rate, we have imaged using a 2-beam condition near the [001] zone axis with the g <200> and <110> vectors. To determine whether loop coalescence occurs and to quantify the final damage taking into consideration possible loop coalescence, the irradiation damage was quantified in two different methods. For this purpose, the samples irradiated at 0.25 dpa were used.

3.2.1. Method A

In this method, the density and the area of the loops were determined from the bright field images. The material, however, was shown to have two loop types (<111> and <100>). Thus, the average areas of the different loop types and their densities have to be found to determine the final damage. To determine the density, the densities of <111> and <100> loops found above at g <200> and <110> vectors were used. In the same quantification zone (area), the total loop area was determined. The average areas (assuming monomodal distributions of individual loop areas) of <111> (A1) and <100> (A2) loops were then determined from the following two equations:

$$D_1^{<200>} \times A1 + D_2^{<200>} \times A2 = A_T^{<200>}$$
$$(\text{for the g} < 200 > \text{ vector})$$

$$D_1^{<110>} \times A1 + D_2^{<110>} \times A2 = A_T^{<110>}$$
$$(\text{for the g} < 110 > \text{ vector})$$

where D_1 and D_2 are the number of <111> and <100> loops respectively in the same quantification area. The number of the loops is simply the density of loops multiplied by the quantification area used. A1 and A2 indicates the average areas of <111> and <100> loops, and A_T is the total loop area for the given g vector. The exponents <110> and <200> indicate the g vectors used. The assumption in this method is that the g vector only affects the intensity of the loops but not their size. High magnification images were used for this purpose.

The total damage was calculated as follows:

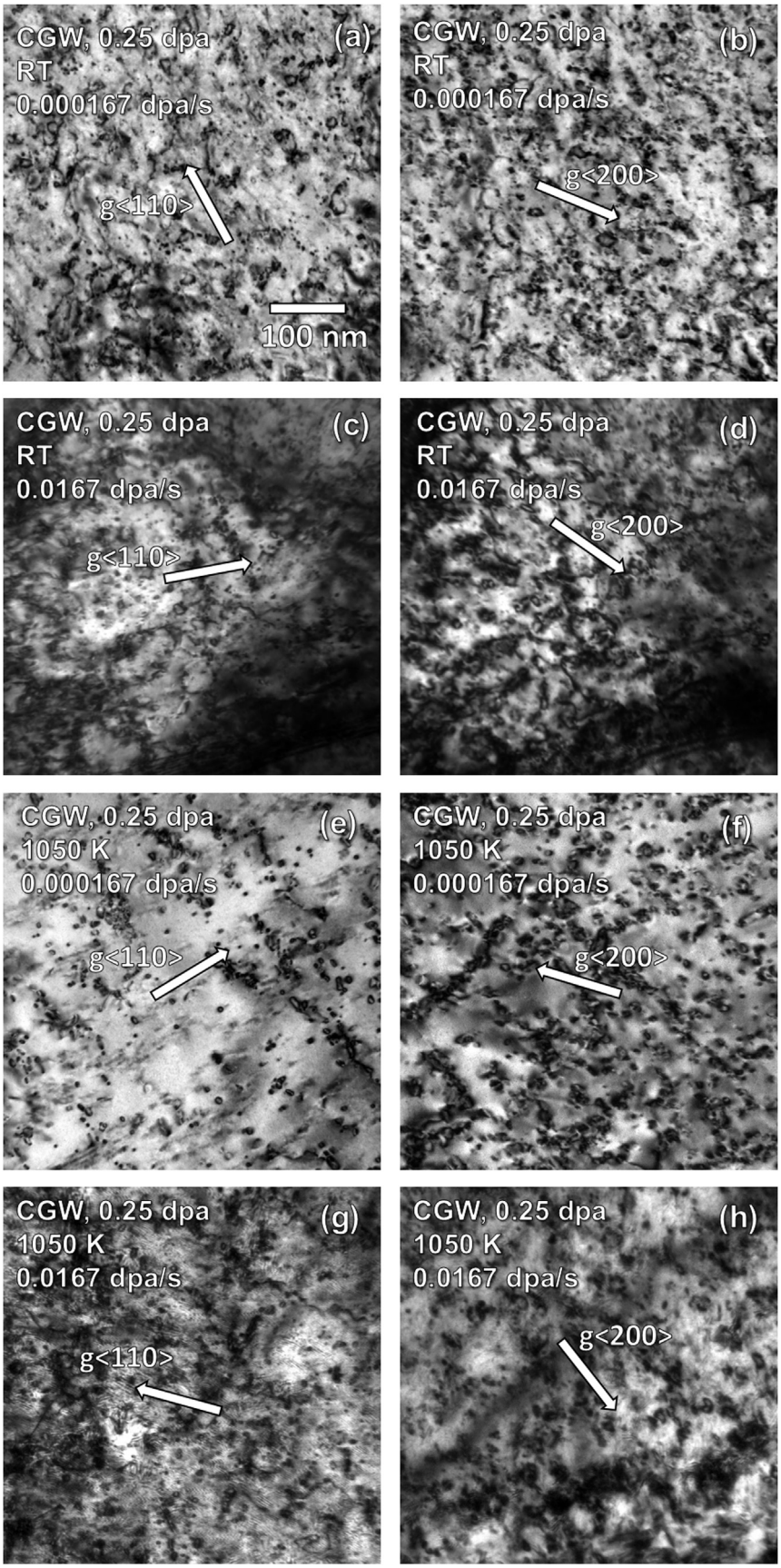

Fig. 2. Bright-field 2-beam TEM images using two beam conditions from the [001] zone axis showing loops in 3 MeV irradiated CGW to final dose of 0.25 dpa: (a), (b) RT irradiation with the low dpa rate of 0.000167 dpa/s using g vectors of <110> and <200> respectively. (c), (d) RT irradiation with the high dpa rate of 0.0167 dpa/s using g vectors of <110> and <200> respectively. (e), (f) 1050 K irradiation with the low dpa rate of 0.000167 dpa/s using g vectors of <110> and <200> respectively. (g), (h) 1050 K irradiation with the high dpa rate of 0.0167 dpa/s using g vectors of <110> and <200> respectively. All images have same scale bar of 100 nm.

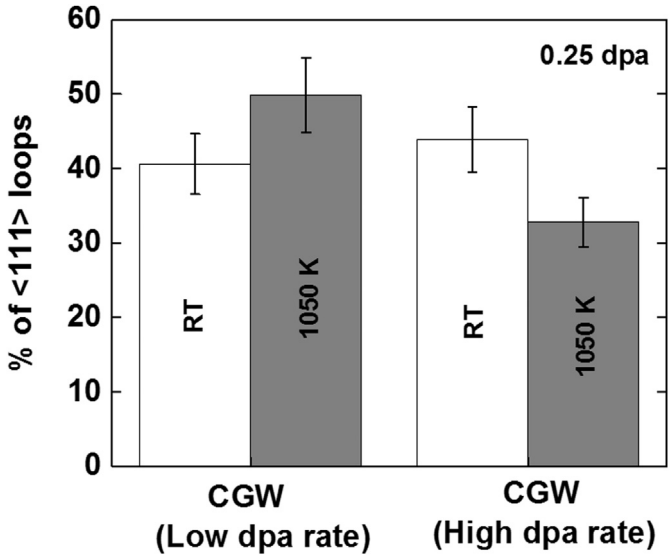

Fig. 3. Percentage of <111> loops for the 3 MeV irradiated CGW to 0.25 dpa at the different irradiation conditions (conditions in Fig. 2). Error bars of 10% are added to describe error in loop counting.

$$D_1{}^T \times A1 + D_2{}^T \times A2 = \text{Total damage}$$

where D_1^T and D_2^T are the total number of <111> and <100> loops, respectively. D_1^T is the same as $D_1^{<200>}$ since all variants of <111> loops are present at the <200> g vector while $D_2^T = 3 \times D_2^{<200>}$ since only one variant of the <100> loops appear at <200> g vector. It should be noted that grains with normal close to [001] zone axis were used to minimize loop glide to the surface (surface proximity effects) [9,77]. Solving the above equations at RT and high temperature at each dpa rate, Fig. 6e was generated. In Fig. 6, the density (a and b), average loop areas (c and d) and total damage (e) were plotted.

3.2.2. Method B

The second method to quantify the microstructural damage is to find the total loop area in the quantified region under a specific 2-beam condition. Utilizing this method, a comparison in the microstructural damage can be obtained between the different conditions but not the total damage (as in Method A) since only one g vector was used. The total area is then divided by the quantified area. Fig. 6f shows the results utilizing method B using the <200> g vector. The damage trend of method A and method B are very close

Table 1
Methods to determine the Burgers vector type on heavy ion irradiated tungsten in previous research.

Work	Irradiation	Method	Temperature	Burgers vector
J.T. Bsswell [45]	100-150 keV heavy self ions and fast neutrons	Field ion microscopy and TEM	RT	Vacancy type <111> and <112> loops on {112} planes
Haussermann et al. [51]	30-60 keV Au^+	TEM (thin foil)	RT	Vacancy type <111> on {110} planes. Few pure edge <110>
Jager and Wilkens [53]	60 keV Au^+	TEM (thin foil)	RT	Vacancy type <111> loops on {110}
Sand et al. [49]	150 keV self ions	MD simulations with D-D and A-T potentials	0 K	<111> and <100> interstitial loops and no vacancy loops with D-D potential. Mainly <111> loops formed with only one <100> loops with A-T potential. One vacancy type <100> loop was seen with the A-T potential.
Setyawan et al. [50]	100 eV-100 keV	MD simulations with modified A-T potential	300, 1025 and 2050 K	Interstitial <111> loops on {111} and {110} planes at 300 and 1025 K. 3D interstitial clusters at 2050 K. <100> vacancy type loops on {100} planes were observed at 300 and 1025 K.
Yi et al. [8]	2 MeV self ion	TEM (bulk samples)	300-1023 K	75-80% <111> loops with 75% of interstitial type at RT. 90% <111> loops with 90% interstitial type at 1023 K and 1.2 dpa
Yi et al. [9]	150 keV self ion	TEM (thin foil)	300-1073 K	~60%<111> loops with ~50% of interstitial type at RT and 1 dpa. ~ 100% <111> loops of ~70% interstitial type at 1073 K and 1dpa. Habit planes were {110} and {111}.
This work	3 MeV Cu^+	TEM (thin foil), average area calculation, analysis of voids	300 and 1050 K	40-50% <111> loops. Most of <100> loops are of vacancy type

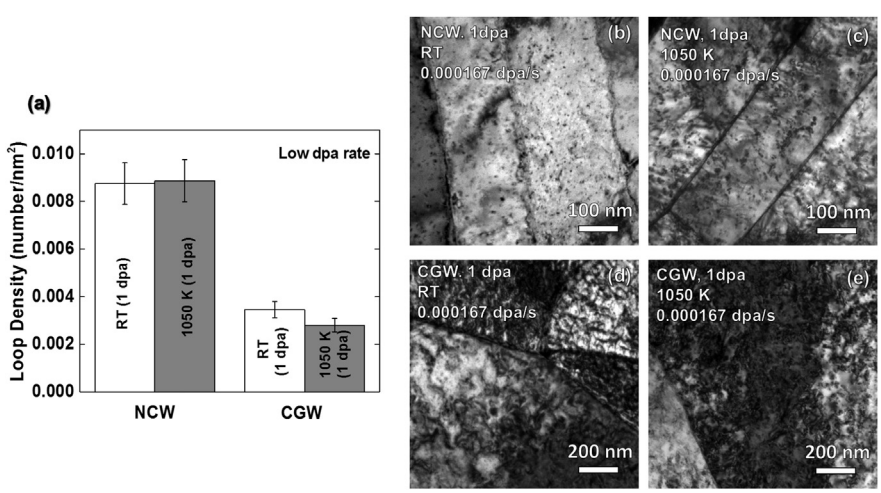

Fig. 4. (a) Loop density (number/nm^2) for 3 MeV irradiated NCW and CGW using the low dpa rate of 0.000167 dpa/s to 1 dpa at RT and 1050 K. Error bars of 10% area added to describe errors from counting the loops. (b), (c), (d) and (e) The corresponding bright-field TEM images.

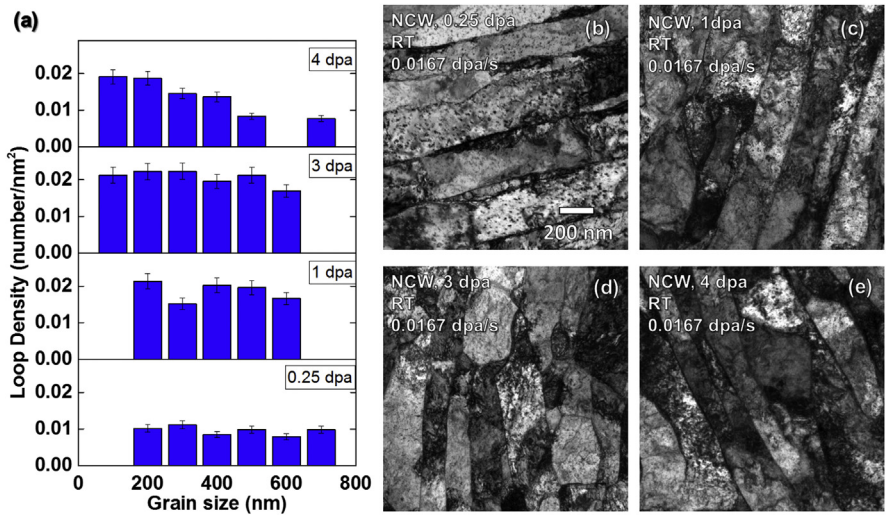

Fig. 5. Loop density (number/nm^2) as a function of grain size for the 3 MeV irradiated NCW using the high dpa rate (0.0167 dpa/s) to different doses at RT. (a) Loop density vs grain size at different doses (Error bars of 10% are added to describe error from counting the loops). (b), (c), (d) and (e) The corresponding bright-field TEM images. All images have the same scale bar of 200 nm.

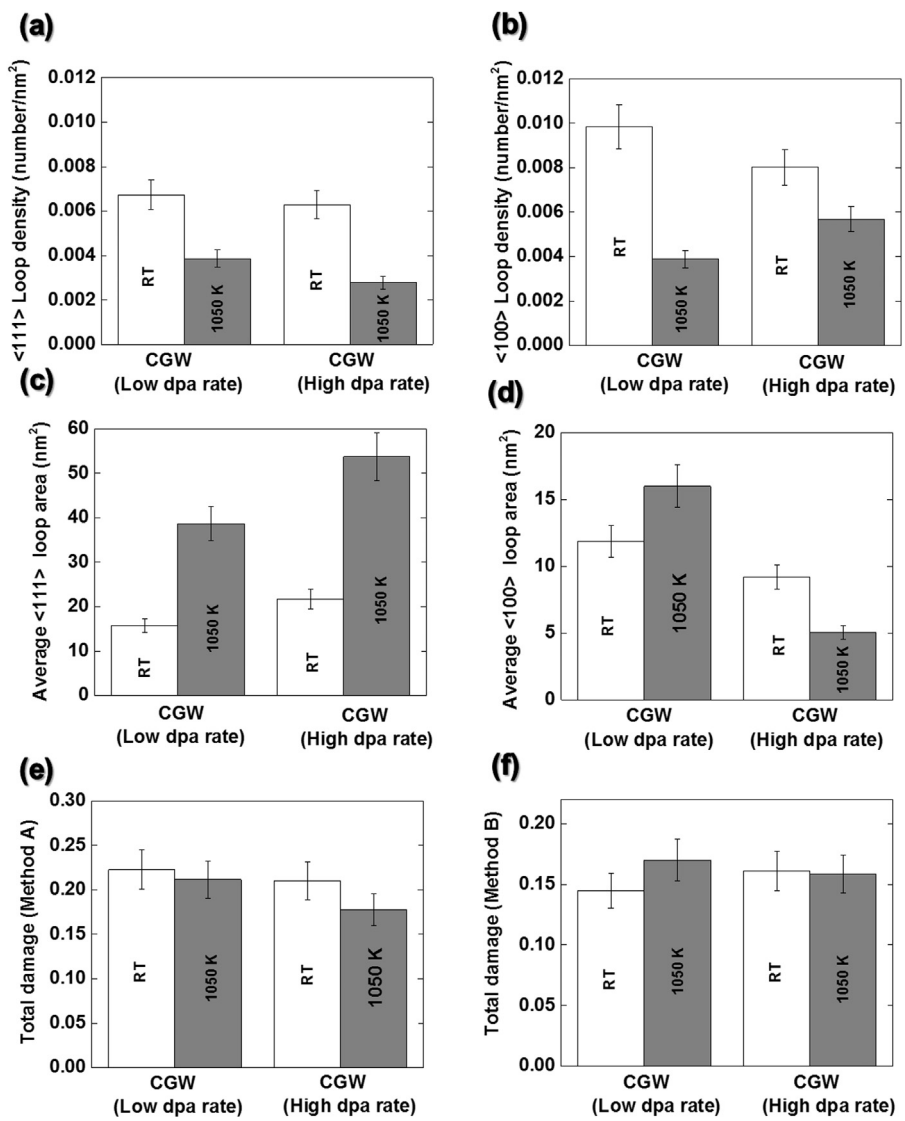

Fig. 6. Damage statistics for the 3 MeV irradiated CGW to 0.25 dpa at the different irradiation conditions (conditions in Fig. 2): (a), (b) Loop density (number/nm^2) for <111> and <100> type loops respectively. (c), (d) Average loop area (nm^2) for <111> and <100> type loops respectively. (e), (f) Total damage quantified using method A and method B respectively. Error bars of 10% are added to describe errors from counting the loops or calculating areas using image J.

proving that method B is an easy way to compare microstructural damage due to irradiation for materials with different generated loop types without performing all the calculations in method A.

It is seen that the microstructural damage quantified using different dpa rates was the same and the damage at RT and 1050 K is nearly the same. Although enhanced annihilation is expected at high temperatures (since vacancy migration does not occur at RT) [78], the loop coalescence rate (which implies higher damage) is also enhanced. The RT experiment corresponds to Stage II recovery in tungsten [7] where interstitial migration occurs and growth of small interstitial loops to TEM resolvable size occurs. The small loops are highly mobile [79]. Under the TEM electron beam, loops in the RT irradiated samples underwent 1-D migration unlike the 1050 K samples. The 1050 K corresponds to stage IV recovery in tungsten which is still subject to debate. It is attributed to the migration of di-vacancies in tungsten or vacancy-impurity complexes [7]. However, as will be illustrated in the void section in this paper, no void coalescence occurred in our samples. The irradiation temperature, 1050 K, is over the temperature range, however, of stage III (723–913 K), where monovacancies start to move and recombination of interstitial is enhanced. At the same time, loops can coalesce at this temperature (enhanced glide) and therefore, larger size loops are expected. The density of the loops will drop and the size of the glissile loops (<111> loops) will increase as shown in Fig. 6c. The total damage from loops, however, for the samples irradiated at RT and 1050 K were found to be the same. This can be understood to occur due to a balance between loop coalescence and the enhanced recombination if voids are not considered. Voids (will be shown below) occurred at 1050 K. Therefore, the total irradiation damage is higher at 1050 K since voids were present in addition to dislocation loops. These voids can occur due to the growth of <100> vacancy loops as will be illustrated below. The difference in dpa rate was also found to have little effect on the total loop damage calculated.

The average areas of <111> and <100> loops calculated (Fig. 6c and d) is not surprising. <111> loops are glissile and their coalescence is always expected at RT and 1050 K. Therefore, their sizes have to be larger than the <100> loops which are relatively sessile [8,80].

3.3. Comparison of microstructure and total irradiation damage of NCW and CGW samples

Since coalescence was shown to affect the total damage, the comparison with the UF and NC sample was to be performed at the same diffraction conditions of the CGW. Since tilting from one g vector to another is very difficult because of the small grain sizes (~100–200 nm), grains imaged with two beam condition (g <200> vectors) were found randomly. Only a few grains were found oriented with the (200) g vector near the [001] zone axis (same conditions as the CGW) (Fig. 7). The quantification of the damage was found by multiplying the loop density with the average loop size (similar to method A but quantifying the <111> and the <100> loops in the NC grains was not possible) or by finding the area fraction (method B). The grain size used in the NC sample was ~180 nm (compared to ~2 μm grain size in the CGW). The results are shown in Fig. 8a and b. From method A, the average loop density and loop area of the NC sample increased with temperature (Fig. 8c and d). The average loop area increased from 14 to 22 nm^2. The increase in irradiation damage with increasing irradiation temperature is indicated by both an increase in loop density (which means that more loops are generated) and loop size through the growth of dislocation loops. The CGW, however, demonstrated a decrease in the density (~50% decrease) and an increase in loop area (from 14 to 32 nm^2) indicating an increase in irradiation damage through mainly loop coalescence. This is a confirmation of the role of grain boundaries in annihilating loops and enhanced interstitial absorption. The total damage, however, was higher in the CGW (~two times) at RT but similar at 1050 K. Several reasons can lead to similar loop damage in the CGW and the NCW at 1050 K despite the higher grain boundary density in the NCW. First, surface effects can contribute to such a trend. In coarse grains, interstitial defects and loops have a higher probability of becoming annihilated at the surface of the foil than at grain boundaries [77]. From Fig. 1, the ratio of the grain boundary area to the surface area of the sample was quantified for the CGW and the NCW. The ratio was ~0.04 for the CGW and 0.46 for NCW (11.5 times higher). Therefore, it is expected that the NCW would have higher irradiation resistance but in this work it is similar (Fig. 8a and b) due to higher annihilation of loops and defects to the surface of the CGW. Second, the NCW showed less void damage. The total damage should include both loop and void damage and in this case, the NCW has improved irradiation resistance. Third, grain boundary sink efficiency can be different in both grades. A similar damage at 1050 K can indicate a role of grain boundary efficiency (different grain boundaries have different sink efficiencies) or that the sink strength of 180 nm grains does not introduce enough radiation tolerance when compared to 1–2 μm grains. It should be mentioned that according to Fig. 1, most of the elongated and small grains in the NCW grades have LAGBs. However, the sink efficiency was shown to depend on the overall grain boundary macroscopic character which includes both the misorientation angle and the grain boundary plane [22,81] which are out of the scope of this paper. To comment on the sink efficiency versus grain boundary density effect, the vacancy profile near a grain boundary was simulated using KMC simulations. Fig. 9 shows the steady state vacancy profile at RT and 1050 K with a dose rate of 10^{-4} dpa/s and a grain size of 50.6 nm. We observe that at RT the concentration of vacancies is slightly larger close to the interface. This is a direct consequence of the fact that the vacancy mobility at this temperature is reduced and the profile follows the inverse of the self-interstitial profile, i.e., the effect of the interface in the vacancy profile is minor. On the other hand, at high temperature, the vacancy concentration decreases close to the GB. Hence, there is a flux of vacancies towards the interface, i.e., vacancy mobility is large enough to explore the whole landscape, including the interface. Nevertheless, both profiles are remarkably flat, which indicates that the recombination in bulk is the dominant process. At high temperature (1050 K), our modeling shows a flux of vacancies towards the interface, which implies higher recombination and should add to the extra interstitial storage at the grain boundaries in the NCW. The fact that our experiments show equal damage in both NCW and CGW might be explained by a larger sink efficiency of the grain boundaries, otherwise, the NCW should present a lower level of damage. In addition, the initial dislocation density in the NCW and the internal stresses due to the machining process can affect defect evolution in the grain matrices. Specifically, severe plastically deformed samples are shown to possess non-equilibrium grain boundaries [82] which can act as enhanced defect sinks compared to their equilibrium counterparts [83]. In addition, Samara et al. have demonstrated that defect clusters were attracted to regions of large stress gradient [84]. Dislocations can also act as biased sinks [85] and can enhance loop coalescence and ordering (raft formation) [86,87].

Coalescence of loops and characterization and quantification challenges even at low dpa (~0.25 dpa) are some issues that need to be overcome to compare the performance of different material grades and evaluate the performance of nanocrystalline materials. Other methods are to be used for this purpose. Recently, the use of nano differential scanning calorimetry techniques to measure the energy absorbed in irradiated materials (stored energy due to

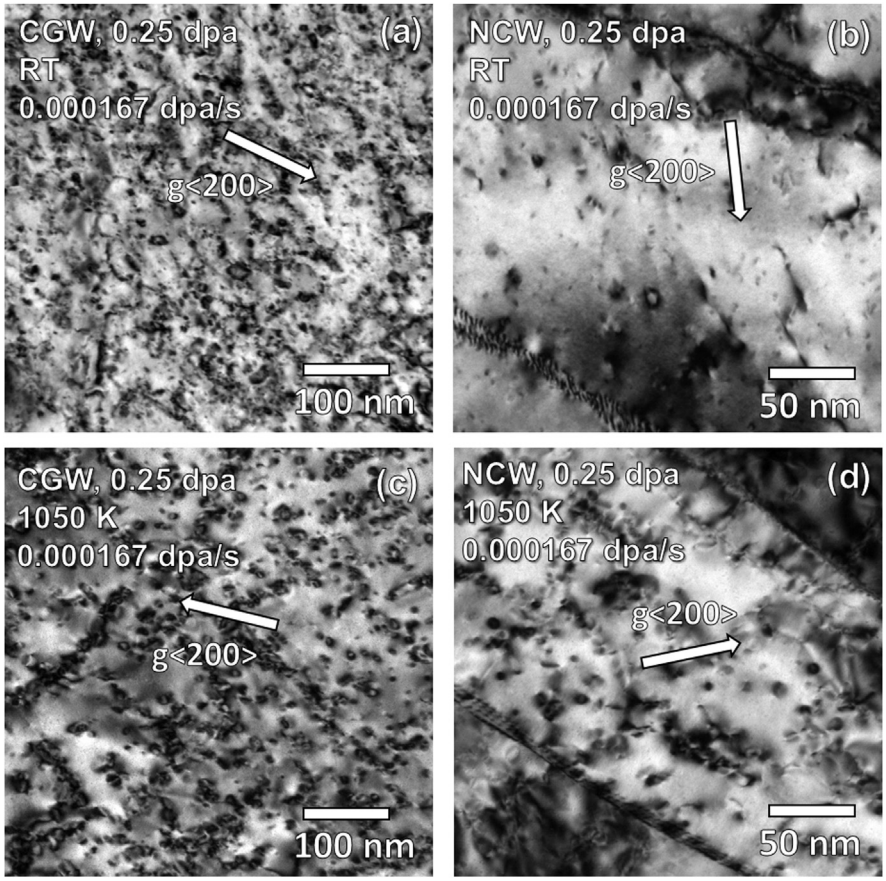

Fig. 7. Bright-field 2-beam TEM images for the 3 MeV irradiated NCW and CGW to 0.25 dpa using dpa rate of 0.000167 dpa/s. (a), (b) RT irradiation for CGW and NCW respectively. (c), (d) 1050 K irradiation for CGW and NCW respectively. Images were taken using the g (200) vector under [001] zone axis.

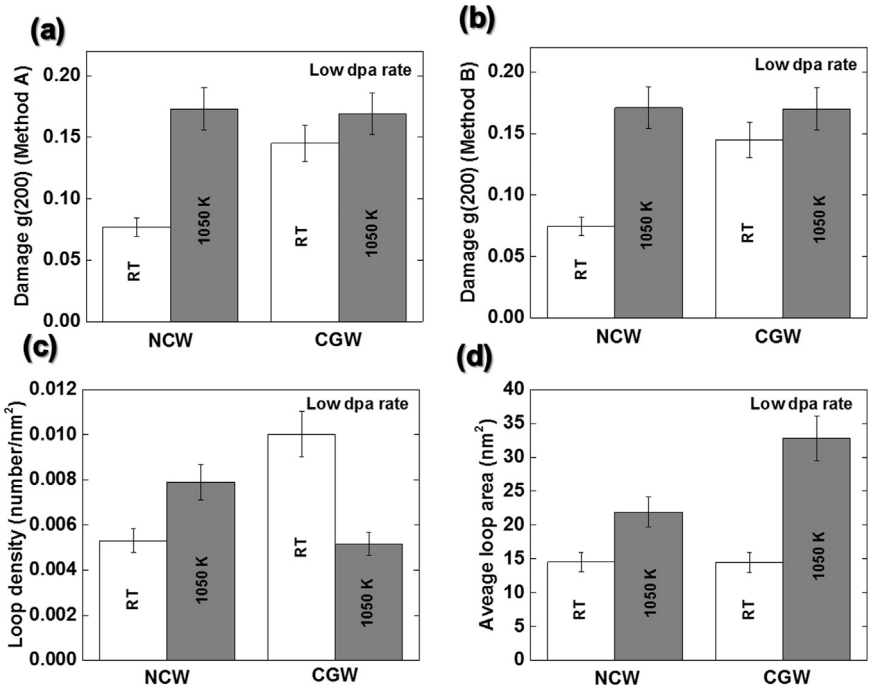

Fig. 8. Total damage comparison of the NCW and CGW under the g <200> 2-beam imaging after 3 MeV irradiation to 0.25 dpa using the low dpa rate of 0.000167 dpa/s. (TEM images are in Fig. 7). (a) Total damage using method A. (b) Total damage using method B. (c), (d) Loop density (number/nm^2) and average loop area (nm^2) respectively that used to calculate the total damage in (a) (Error bars of 10% area added to describe errors from counting the loops or calculating areas using image J.

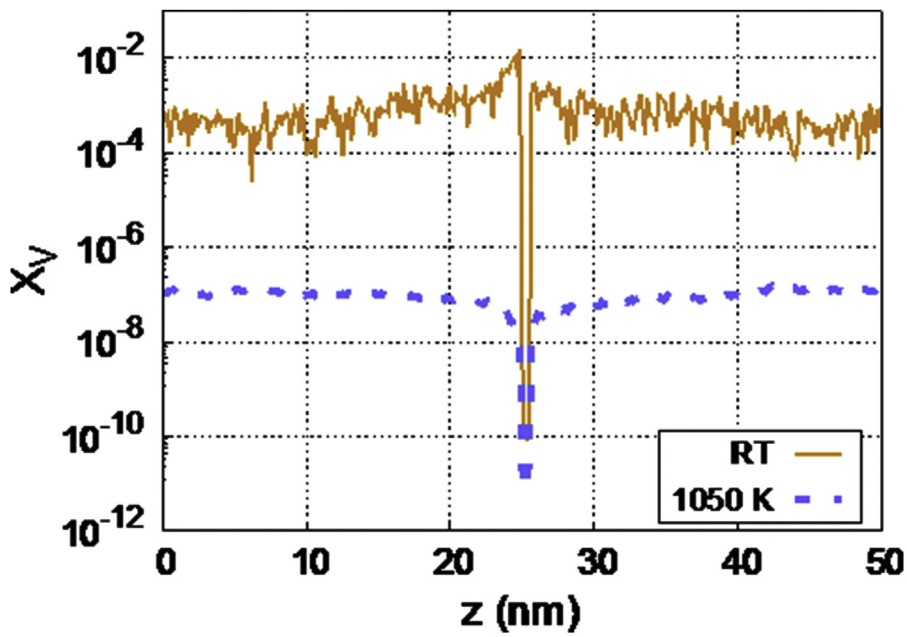

Fig. 9. Vacancy distribution in W at steady-state at RT and 1050 K with a dose rate of 10^{-4} dpa/s and a grain size of 50.6 nm.

irradiation generated defects) was suggested to characterize irradiation damage in irradiated materials [88]. Property response of irradiated materials can also act as a measure of the irradiation damage. Nanomechanical tests on irradiated samples can provide a measure of the damage by examining the change in hardness. The damage from void formation and loop formation can be identified from these tests by systematical procedures. Nanoindentation work on the irradiated samples and correlation with apparent damage in the TEM images is ongoing.

3.4. Rafting

Fig. 10 shows an interesting phenomena, dislocation loop rafting, that was observed in various BCC metals under neutron and heavy ion irradiation (both thin foils and bulk) [8,48,54,89,90]. The mechanism for rafting is still up for debate [43,54,55,86]. Detailed Burgers loop analysis of the loops in these rafts (presented elsewhere) showed that the loops in the rafts are of one Burgers vector variant with no grain orientation dependence as presented in other published work [9]. As shown in Fig. 10, the loop rafting was observed at RT and 1050 K unlike most other studies which observed it at high temperatures only. The one loop variant of these rafts and their observation at both high and low temperatures (where vacancies do not migrate), contradicted several mechanism and confirmed the mechanism of Wen et al. [86] who demonstrated that loop glide and rotation to match the same Burgers vector variant are essential to form these rafts.

3.5. Void formation, swelling and effect of grain boundary density

Void formation in the samples was characterized and quantified. At RT, very small voids were observed at high magnifications. These were very hard to distinguish from the background. At RT, thermal vacancy migration in tungsten is not possible (migration energy of vacancy in tungsten is ~1.7 eV) [91]. Such voids could then be a result of vacancy clustering from the collision cascade. At 1050 K, void sizes increased to ~2.1 nm. Void growth occurred up to 1 dpa. There are various suggested mechanisms for the growth of voids at

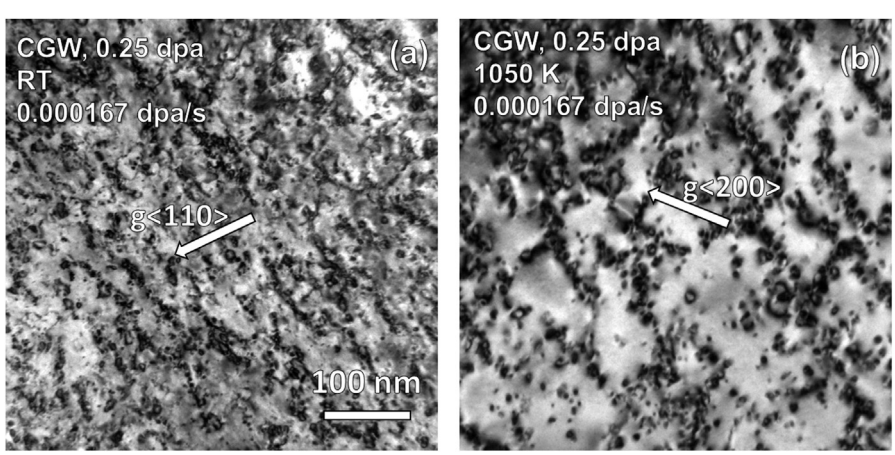

Fig. 10. Bright-field TEM images of the 3 MeV irradiated CGW to 0.25 dpa using the low dpa rate of 0.000167 dpa/s showing loop rafting. (a) RT irradiation with loop rafting appears using the g <110> vector and (b) 1050 K irradiation with loop rafting appear using the g <200> vector. Imaging was performed using the [001] zone axis.

high temperatures. Void growth was demonstrated to occur from vacancy loops to release stresses from system [92]. Vacancy loop growth was also modelled to occur via loop-loop and loop-void elastic interactions and monovacancy migration [93]. Vacancy loops were observed experimentally under similar irradiation conditions on W [8]. MD simulations by Setyawan et al. [50] demonstrated that at 300 K and 1025 K (similar to the irradiation temperatures in this study), vacancy loops and small cavities are created directly from the collision cascade. These loops were mostly of <100> type loops which are relatively sessile loops. Our average value determination of the <111> and <100> loops (Fig. 3) demonstrated small areas of the sessile <100> loops as expected. As previously discussed, we then attributed the small loops to be of <100> type. The work by Yi et al. showed no <100> loops, but loops smaller than 4 nm were not analyzed. Gilbert et al. [94] demonstrated that vacancy loops are metastable structures which tend to evolve into voids at modest temperature via diffusion of monovacancies. At 1025 K, vacancy migration is present in tungsten and such vacancy loops can capture migrating vacancies to grow. The presence of interstitial biased microstructure such as dislocations and interstitial dislocation loops and rafting favor the formation of voids through supersaturation of vacancies [55]. Fig. 11 shows bright field TEM images of the voids at different irradiation conditions on both tungsten grades used in this study. The voids showed uniform distribution across the different grains. On imaging an inclined grain boundary (Fig. 11a), voids were shown to be present but with similar sizes and distributions to the ones in the grain matrices suggesting their formation from the collision cascades as mentioned earlier. Void damage produces swelling. Swelling was quantified in the NCW and the CGW (Fig. 12). The swelling at high dpa rate in the CGW is plotted in Fig. 12b. The swelling decreased after 0.25 dpa irradiation due to the shrinkage of voids (Fig. 12c). Such shrinkage is an agreement with the work by Evans et al. and a validation of his theory [56] as described before. This can also confirm our previous analysis where vacancy loops were shown to be very small in the 0.25 dpa irradiated samples (voids were still growing). After that, void shrinkage could occur due to an increase in vacancy loop sizes that nucleate at the void sites. To study the effect of grain density on the swelling percentage at 0.25 and 1 dpa, the void swelling was also quantified in the NC tungsten. Fig. 12a shows the comparison at different irradiation conditions. Overall, at low dpa rate, the NC tungsten showed better swelling resistance when compared to CGW. At high dpa rate, the comparison was performed only at 0.25 dpa. No difference in the swelling percentage is observed. Since these voids grow while absorbing vacancies, the high dpa rate offers less time for vacancy migration to occur and therefore no difference was observed between the NC and the CGW samples.

Swelling vs. grain size in the NC sample (both the NC and UF regimes were studied) are shown in Fig. 12d for the low dpa rate. No effect of individual grain sizes was observed confirming the uniform distribution of the voids in the TEM micrograph. In addition, no denuded zones were observed in any of the samples. We attribute that to the fact that these voids nucleated from the sessile <100> vacancy loops which are, in turn, directly nucleated from the heavy cascades as discussed before, and not from vacancy migration and coalescence where vacancy absorption by the boundaries can create a vacancy profile and create a void denuded zone near the grain boundaries [95].

3.6. Surface effects

Since irradiations were performed on thin foils, the vicinity of the free surface can affect defect densities due to surfaces acting as sinks. Such effect was studied by Li et al. [77] and Ferroni et al. [96]. Ferroni et al., through glide and climb dislocation modeling in tungsten, reached a conclusion that dislocation loops interact strongly with surfaces for depths that are less than three times the size of the loop which can create a denuded zone near the surface (with smaller size due to interaction of loops with other small clusters or impurities). From SRIM, the damage profile of 1 MeV Cu^{+} goes through the 100 nm thickness of the sample. Taking the CGW tungsten as an example, and using the average loop sizes at RT and 1050 K shown in Fig. 8d (4.5 and 6.5 nm respectively), approximately 13.5% and 19.5% of the damage profile is within the near surface region (neglecting other traps such as small clusters and impurities). Moreover, since the glissile interstitial loops are of <111> Burgers vector, quantification of loop densities using {001} zone axis (used in this study) should minimize loop interactions with the surface. Yi et al. [8] studied the influence of grain orientation on damage of 2 MeV self-ion irradiated tungsten materials and reached a conclusion that grains of {001} orientation are more likely to represent neutron irradiated specimen of equivalent dose and temperature. Therefore, trends of Burgers vector type, loop density and total damage of the same sample type will not be affected. When comparing NCW to CGW, surface effects (where surfaces act as defect sinks) are expected to play more significant role in large grains (CGW) due to the longer diffusion path of the

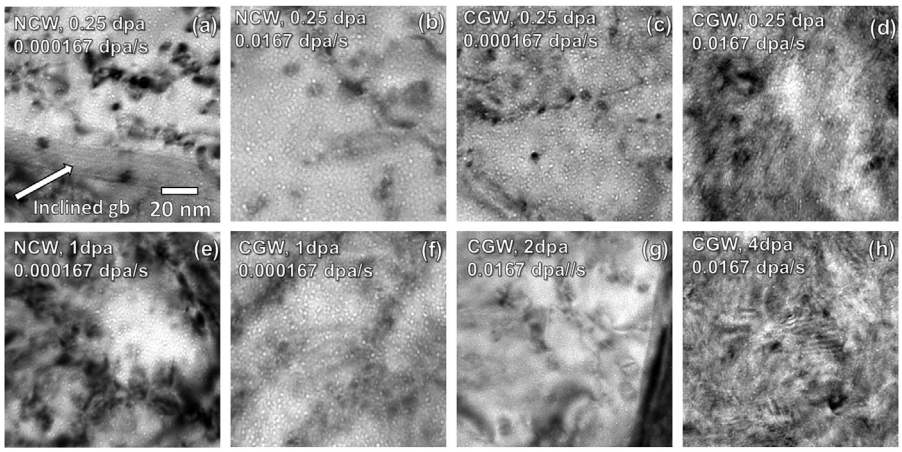

Fig. 11. Bright-field Fresnel (underfocused) images of voids in the 3 MeV and 1050 K irradiated NCW and CGW at different irradiation conditions. (a), (b) 0.25 dpa NCW using the dpa rates of 0.000167 dpa/s and 0.0167 dpa/s respectively. (c), (d) 0.25 dpa CGW using the dpa rates of 0.000167 dpa/s and 0.0167 dpa/s respectively. (e), (f) 1 dpa of NCW and CGW respectively using the low dpa rate of 0.000167 dpa/s. (g), (h) CGW irradiated to 2 dpa and 4 dpa respectively using the high dpa rate of 0.0167 dpa/s.

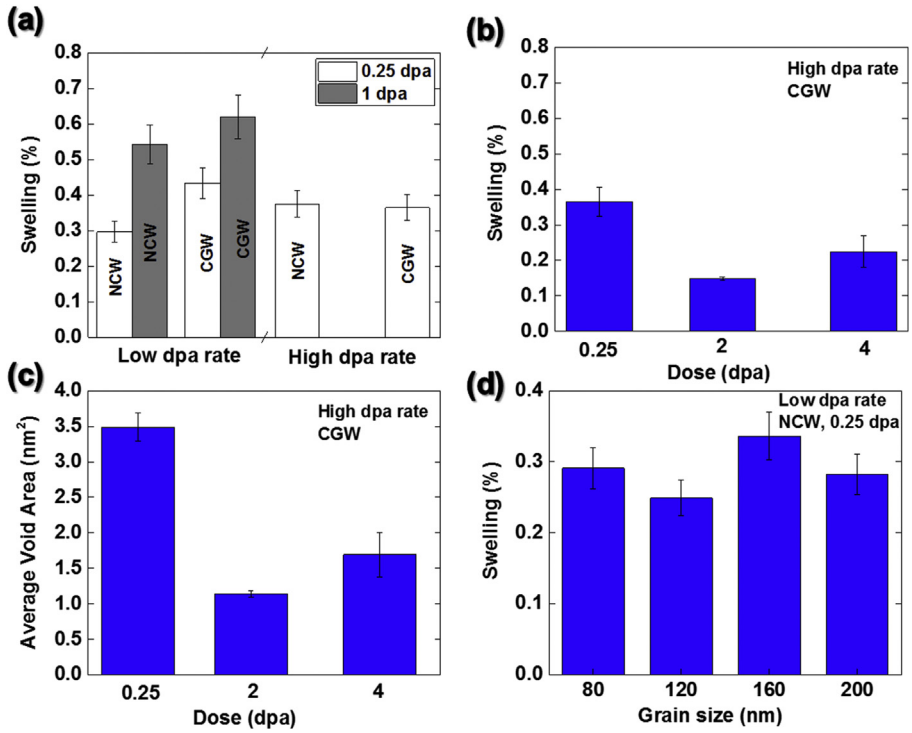

Fig. 12. (a) Swelling percentage comparisons of the 3 MeV and 1050 K irradiated NCW and CGW at similar irradiation conditions. (b) Swelling vs dpa for the CGW irradiated using the high dpa rate of 0.0167 dpa/s. (c) Average void area (nm^2) used to calculate swelling percentage in (b). (d) Swelling percentage for the 0.25 dpa irradiated NCW using the low dpa rate of 0.000167 dpa/s. Error bars in swelling are taken to be the standard error of the mean (SEM).

defects to the grain boundaries, and therefore, it is fair to assume that defect quantification values in the CGW are more underestimated than the NCW as stated above.

4. Summary and conclusions

Two tungsten grades CGW and NCW were irradiated with 3 MeV Cu^+ at RT and 1050 K to different dpa values (0.25–4 dpa) using two different dpa rates (0.0167 dpa/s and 0.000167 dpa/s). Loop Burgers vector, loop density measurements and average loop areas were determined. The total microstructural damage was quantified using two methods where loop density and average area were used in the first method and loop area fraction in the grain matrices was used in the second one. Voids were observed at 1050 K and swelling was determined. The damage from loops and voids was compared in both tungsten grades and the conclusions are as follows:

1 At both temperatures (RT and 1050 K), both <111> and <100> Burgers vector loops are observed with <100> loops suggested to be of vacancy type.
2 Quantification of loop density exclusively does not give a measure of irradiation damage. For doses over 0.25 dpa, the CGW demonstrated loop coalescence (larger average loop area but lower density than NCW).
3 Total damage quantification using average loop area and average loop density (for both <111> and <100> loops) demonstrated similar trend to the average fraction of loop areas in the grain matrices. Irradiation damage by loop formation was shown to be the same from two different dpa rates (100 times different). Comparing the loop density and average areas for both grades at 0.25 dpa for both dpa rates and both temperatures showed that the NCW did not demonstrate loop coalescence at this dose while CGW demonstrated significant coalescence. Loop density as a function of grain size in the nanocrystalline and ultrafine regime demonstrated similar values. The average loop areas of <100> loops were shown to be very small at 0.25 dpa suggesting these loops result directly from the cascades and confirming their sessile behavior. Such loops can hardly be distinguished using weak beam methods in the TEM (which needs high exposure times).
4 NCW with grain sizes of 150–200 nm was shown to have lower loop damage at RT but similar loop damage at 1050 K to CGW. The similar damage at 1050 K was attributed to the increase in surface effects in the CGW, vacancy loop growth to voids and the enhanced sink efficiency in the CGW as concluded from the vacancy distribution profiles in tungsten at RT and 1050 K.
5 NCW with grain sizes ranging from 50 to 600 nm was shown to have less void swelling at both dpa rates than CGW. The occurrence of voids at higher temperatures with no denuded zone formation suggests void growth from local sites. These sites are thought to be the vacancy loop sites which grow through vacancy absorption at high temperatures. Swelling determination as a function of grain size in the nanocrystalline and ultrafine regime demonstrated similar values.
6 Voids were shown to shrink at large dpa values which was explained to occur due to growth of vacancy loops on the void sites.

Quantification of microstructural damage due to irradiation is a complex process and can be plagued with human and experimental errors. At high dpa values, significant coalescence and damage (loop tangling, raftings, etc.) occurs, which leads to significant challenges in determining the loop densities and sizes. This work showed that coalescence in CGW can occur at dpa values as low as 0.25 dpa, therefore, loop density comparisons (the most common method) are misleading. Denuded zones were often believed to

give insight on sink efficiencies and irradiation resistance. This work showed that although no denuded zone forms, the NCW showed enhanced irradiation resistance regarding loop damage (at RT) and void damage (swelling at high temperatures). Therefore, other methods are to be used to quantify irradiation damage in nuclear materials at high dpa values. Methods like measuring the energy stored due to irradiation damage or correlating the nanomechanical properties with irradiation conditions (ongoing work) can be reliable alternatives to comparing loop densities especially when comparing different materials or different grain sizes. Comparison of very small grain sizes (<50 nm) with CGW at the same imaging conditions in the TEM is challenging but should provide essential data on irradiation resistance of NCW materials provided that the grains quantified have similar grain boundaries with similar characters (or sink efficiency) which requires a very complex characterization process.

Acknowledgement

Research presented in this article was supported by the Laboratory Directed Research and Development program of Los Alamos National Laboratory under project number 20160674PRD3. We gratefully acknowledge the support of the U.S. Department of Energy through the LANL/LDRD Program and the G. T. Seaborg Institute for this work.

Appendix A. Supplementary data

Supplementary data related to this article can be found at https://doi.org/10.1016/j.actamat.2018.02.035.

References

[1] G. Federici, C.H. Skinner, J.N. Brooks, J.P. Coad, C. Grisolia, A.A. Haasz, A. Hassanein, V. Philipps, C.S. Pitcher, J. Roth, Plasma-material interactions in current tokamaks and their implications for next step fusion reactors, Nucl. Fusion 41 (12) (2001) 1967.
[2] S.J. Zinkle, L.L. Snead, Designing radiation resistance in materials for fusion energy, Annu. Rev. Mater. Res. 44 (2014) 241–267.
[3] J. Knaster, A. Moeslang, T. Muroga, Materials research for fusion, Nat. Phys. 12 (5) (2016) 424–434.
[4] M. Jenkins, Characterisation of radiation-damage microstructures by TEM, J. Nucl. Mater. 216 (1994) 124–156.
[5] M.L. Jenkins, M.A. Kirk, Characterisation of Radiation Damage by Transmission Electron Microscopy, CRC Press, 2000.
[6] O. El-Atwani, J. Hinks, G. Greaves, S. Gonderman, T. Qiu, M. Efe, J. Allain, In-situ TEM observation of the response of ultrafine-and nanocrystalline-grained tungsten to extreme irradiation environments, Sci. Rep. 4 (2014).
[7] F. Ferroni, X. Yi, K. Arakawa, S.P. Fitzgerald, P.D. Edmondson, S.G. Roberts, High temperature annealing of ion irradiated tungsten, Acta Mater. 90 (2015) 380–393.
[8] X. Yi, M.L. Jenkins, K. Hattar, P.D. Edmondson, S.G. Roberts, Characterisation of radiation damage in W and W-based alloys from 2MeV self-ion near-bulk implantations, Acta Mater. 92 (2015) 163–177.
[9] X. Yi, M.L. Jenkins, M.A. Kirk, Z. Zhou, S.G. Roberts, In-situ TEM studies of 150 keV W+ ion irradiated W and W-alloys: damage production and microstructural evolution, Acta Mater. 112 (2016) 105–120.
[10] O. El-Atwani, A. Suslova, T. Novakowski, K. Hattar, M. Efe, S. Harilal, A. Hassanein, In-situ TEM/heavy ion irradiation on ultrafine-and nanocrystalline-grained tungsten: effect of 3MeV Si, Cu and W ions, Mater. Char. 99 (2015) 68–76.
[11] M. Toulemonde, C. Dufour, E. Paumier, Transient thermal process after a high-energy heavy-ion irradiation of amorphous metals and semiconductors, Phys. Rev. B 46 (22) (1992) 14362.
[12] Z.G. Wang, C. Dufour, E. Paumier, M. Toulemonde, The Se sensitivity of metals under swift-heavy-ion irradiation: a transient thermal process, J. Phys. Condens. Matter 6 (34) (1994) 6733.
[13] S.J. Zinkle, G. Was, Materials challenges in nuclear energy, Acta Mater. 61 (3) (2013) 735–758.
[14] V. Philipps, Tungsten as material for plasma-facing components in fusion devices, J. Nucl. Mater. 415 (1) (2011) S2–S9.
[15] S. Kajita, W. Sakaguchi, N. Ohno, N. Yoshida, T. Saeki, Formation process of tungsten nanostructure by the exposure to helium plasma under fusion relevant plasma conditions, Nucl. Fusion 49 (9) (2009) 095005.
[16] O. El-Atwani, M. Efe, B. Heim, J.P. Allain, Surface damage in ultrafine and multimodal grained tungsten materials induced by low energy helium irradiation, J. Nucl. Mater. 434 (1–3) (2013) 170–177.
[17] M.J. Baldwin, R.P. Doerner, Formation of helium induced nanostructure 'fuzz'on various tungsten grades, J. Nucl. Mater. 404 (3) (2010) 165–173.
[18] H. Kurishita, H. Arakawa, S. Matsuo, T. Sakamoto, S. Kobayashi, K. Nakai, G. Pintsuk, J. Linke, S. Tsurekawa, V. Yardley, Development of nanostructured tungsten based materials resistant to recrystallization and/or radiation induced embrittlement, Mater. Trans. 54 (4) (2013) 456–465.
[19] T. Byun, K. Farrell, Irradiation hardening behavior of polycrystalline metals after low temperature irradiation, J. Nucl. Mater. 326 (2) (2004) 86–96.
[20] M. Efe, O. El-Atwani, Y. Guo, D.R. Klenosky, Microstructure refinement of tungsten by surface deformation for irradiation damage resistance, Scripta Mater. 70 (2014) 31–34.
[21] S. Wurster, N. Baluc, M. Battabyal, T. Crosby, J. Du, C. García-Rosales, A. Hasegawa, A. Hoffmann, A. Kimura, H. Kurishita, Recent progress in R&D on tungsten alloys for divertor structural and plasma facing materials, J. Nucl. Mater. 442 (1) (2013) S181–S189.
[22] W. Han, M. Demkowicz, E. Fu, Y. Wang, A. Misra, Effect of grain boundary character on sink efficiency, Acta Mater. 60 (18) (2012) 6341–6351.
[23] M.A. Tschopp, K. Solanki, F. Gao, X. Sun, M.A. Khaleel, M. Horstemeyer, Probing grain boundary sink strength at the nanoscale: energetics and length scales of vacancy and interstitial absorption by grain boundaries in α-Fe, Phys. Rev. B 85 (6) (2012) 064108.
[24] H. Gleiter, Grain boundaries as point defect sources or sinks—diffusional creep, Acta Metall. 27 (2) (1979) 187–192.
[25] B.N. Singh, T. Leffers, W. Green, M. Victoria, Nucleation of helium bubbles on dislocations, dislocation networks and dislocations in grain boundaries during 600 MeV proton irradiation of aluminium, J. Nucl. Mater. 125 (3) (1984) 287–297.
[26] X.-M. Bai, A.F. Voter, R.G. Hoagland, M. Nastasi, B.P. Uberuaga, Efficient annealing of radiation damage near grain boundaries via interstitial emission, Science 327 (5973) (2010) 1631–1634.
[27] T.D. Shen, S. Feng, M. Tang, J.A. Valdez, Y. Wang, K.E. Sickafus, Enhanced radiation tolerance in nanocrystalline MgGa 2 O 4, Appl. Phys. Lett. 90 (26) (2007), 263115-263115-3.
[28] N. Nita, R. Schaeublin, M. Victoria, Impact of irradiation on the microstructure of nanocrystalline materials, J. Nucl. Mater. 329 (2004) 953–957.
[29] Y. Chimi, A. Iwase, N. Ishikawa, M. Kobiyama, T. Inami, S. Okuda, Accumulation and recovery of defects in ion-irradiated nanocrystalline gold, J. Nucl. Mater. 297 (3) (2001) 355–357.
[30] Y. Chen, J. Li, K. Yu, H. Wang, M. Kirk, M. Li, X. Zhang, In situ studies on radiation tolerance of nanotwinned Cu, Acta Mater. 111 (2016) 148–156.
[31] C. Sun, M. Song, K. Yu, Y. Chen, M. Kirk, M. Li, H. Wang, X. Zhang, In situ Evidence of defect cluster absorption by grain boundaries in Kr ion irradiated nanocrystalline Ni, Metall. Mater. Trans. 44 (4) (2013) 1966–1974.
[32] O. El-Atwani, J. Hinks, G. Greaves, J. Allain, S. Maloy, Grain size threshold for enhanced irradiation resistance in nanocrystalline and ultrafine tungsten, Materials Research Letters (2017) 1–7.
[33] O. El-Atwani, J. Nathaniel, A. Leff, B. Muntifering, J. Baldwin, K. Hattar, M. Taheri, The role of grain size in He bubble formation: implications for swelling resistance, J. Nucl. Mater. 484 (2017) 236–244.
[34] J. Li, K. Yu, Y. Chen, M. Song, H. Wang, M. Kirk, M. Li, X. Zhang, In situ study of defect migration kinetics and self-healing of twin boundaries in heavy ion irradiated nanotwinned metals, Nano Lett. 15 (5) (2015) 2922–2927.
[35] S. Wurster, R. Pippan, Nanostructured metals under irradiation, Scripta Mater. 60 (12) (2009) 1083–1087.
[36] O. El-Atwani, J. Nathaniel II, A. Leff, J. Baldwin, K. Hattar, M. Taheri, Evidence of a temperature transition for denuded zone formation in nanocrystalline Fe under He irradiation, Mat. Res. Lett. (2016) 1–6.
[37] O. El-Atwani, J. Nathaniel, A. Leff, K. Hattar, M. Taheri, Direct observation of sink-dependent defect evolution in nanocrystalline iron under irradiation, Sci. Rep. 7 (2017).
[38] I. Beyerlein, M. Demkowicz, A. Misra, B. Uberuaga, Defect-interface interactions, Prog. Mater. Sci. 74 (2015) 125–210.
[39] R. Nelson, D. Mazey, J. Hudson, The use of ion accelerators to simulate fast neutron-induced voidage in metals, J. Nucl. Mater. 37 (1) (1970) 1–12.
[40] R. Averback, R. Benedek, K. Merkle, Ion-irradiation studies of the damage function of copper and silver, Phys. Rev. B 18 (8) (1978) 4156.
[41] Y. Zheng, Y. Zuo, D. Yuan, D. Zhou, Y. Xu, P. Fan, J. Zhu, Z. Wang, S. Zhu, Investigation of radiation damage in stainless steel, tungsten and tantalum by heavy ion irradiations, Nucl. Phys. 834 (1–4) (2010) 761c–763c.
[42] G.L. Kulcinski, J. Laidler, D. Doran, Simulation of high fluence fast neutron damage with heavy ion bombardment, Radiat. Eff. 7 (3–4) (1971) 195–202.
[43] S. Dudarev, K. Arakawa, X. Yi, Z. Yao, M. Jenkins, M. Gilbert, P. Derlet, Spatial ordering of nano-dislocation loops in ion-irradiated materials, J. Nucl. Mater. 455 (1) (2014) 16–20.
[44] A. Dunn, R. Dingreville, L. Capolungo, Multi-scale simulation of radiation damage accumulation and subsequent hardening in neutron-irradiated α-Fe, Model. Simulat. Mater. Sci. Eng. 24 (1) (2015), 015005.
[45] J. Buswell, Vacancy damage in heavy ion and neutron-irradiated tungsten, Phil. Mag. 22 (178) (1970) 787–802.
[46] Y. Oya, M. Shimada, M. Kobayashi, T. Oda, M. Hara, H. Watanabe, Y. Hatano, P. Calderoni, K. Okuno, Comparison of deuterium retention for ion-irradiated and neutron-irradiated tungsten, Phys. Scripta 2011 (T145) (2011), 014050.
[47] O. Ogorodnikova, B. Tyburska, V.K. Alimov, K. Ertl, The influence of radiation

damage on the plasma-induced deuterium retention in self-implanted tungsten, J. Nucl. Mater. 415 (1) (2011) S661–S666.
[48] Z. Zhang, K. Yabuuchi, A. Kimura, Defect distribution in ion-irradiated pure tungsten at different temperatures, J. Nucl. Mater. 480 (2016) 207–215.
[49] A. Sand, S. Dudarev, K. Nordlund, High-energy collision cascades in tungsten: dislocation loops structure and clustering scaling laws, EPL (Europhysics Letters) 103 (4) (2013), 46003.
[50] W. Setyawan, G. Nandipati, K.J. Roche, H.L. Heinisch, B.D. Wirth, R.J. Kurtz, Displacement cascades and defects annealing in tungsten, Part I: defect database from molecular dynamics simulations, J. Nucl. Mater. 462 (2015) 329–337.
[51] F. Häussermann, M. Rühle, M. Wilkens, Black-white contrast figures from small dislocation loops II, Appl. First Order sol. Small Loops ion-irr. Tungsten Foils, Physica Status Solidi (b) 50 (2) (1972) 445–457.
[52] F. Häussermann, Analysis of Dislocation Loops in Tungsten Produced by 60 KeV Ion Irradiation, Max-Planck-Institut fuer Metallforschung, Stuttgart, 1972.
[53] W. Jäger, M. Wilkens, Formation of vacancy-type dislocation loops in tungsten bombarded by 60 keV Au ions, Phys. Status Solidi. (a) 32 (1) (1975) 89–100.
[54] J. Brimhall, B. Mastel, Neutron irradiated molybdenum-relationship of microstructure to irradiation temperature, Radiat. Eff. 3 (2) (1970) 203–215.
[55] V. Sikka, J. Moteff, "Rafting" in neutron irradiated tungsten, J. Nucl. Mater. 46 (2) (1973) 217–219.
[56] J. Evans, Radiation-induced shrinkage of voids in molybdenum and TZM, Nature 278 (5706) (1979) 728–729.
[57] Q. Wei, T. Jiao, K. Ramesh, E. Ma, L. Kecskes, L. Magness, R. Dowding, V. Kazykhanov, R. Valiev, Mechanical behavior and dynamic failure of high-strength ultrafine grained tungsten under uniaxial compression, Acta Mater. 54 (1) (2006) 77–87.
[58] Q. Wei, H. Zhang, B. Schuster, K. Ramesh, R. Valiev, L. Kecskes, R. Dowding, L. Magness, K. Cho, Microstructure and mechanical properties of super-strong nanocrystalline tungsten processed by high-pressure torsion, Acta Mater. 54 (15) (2006) 4079–4089.
[59] J.F. Ziegler, M.D. Ziegler, J.P. Biersack, SRIM–the stopping and range of ions in matter (2010), Nucl. Instrum. Methods Phys. Res. Sect. B Beam Interact. Mater. Atoms 268 (11) (2010) 1818–1823.
[60] P. Jung, in: H. Ullmaier (Ed.), Atomic Defects in Metals (Landolt-bornstein New Series III/25), Springer, Berlin, 1991.
[61] E. Elcock, Vacancy diffusion in ordered alloys, Proc. Phys. Soc. 73 (2) (1959) 250.
[62] E. Elcock, C. McCombie, Vacancy diffusion in binary ordered alloys, Phys. Rev. 109 (2) (1958) 605.
[63] A.B. Bortz, M.H. Kalos, J.L. Lebowitz, A new algorithm for Monte Carlo simulation of Ising spin systems, J. Comput. Phys. 17 (1) (1975) 10–18.
[64] D.T. Gillespie, A general method for numerically simulating the stochastic time evolution of coupled chemical reactions, J. Comput. Phys. 22 (4) (1976) 403–434.
[65] D.T. Gillespie, Exact stochastic simulation of coupled chemical reactions, J. Phys. Chem. 81 (25) (1977) 2340–2361.
[66] C. Becquart, B. Wirth, Kinetic Monte Carlo simulations of irradiation effects, in: R.J.M. Konings (Ed.), Comprehensive Nuclear Materials, 2012.
[67] K. Yabuuchi, M. Saito, R. Kasada, A. Kimura, Neutron irradiation hardening and microstructure changes in Fe–Mn binary alloys, J. Nucl. Mater. 414 (3) (2011) 498–502.
[68] M. Jenkins, Z. Yao, M. Hernández-Mayoral, M. Kirk, Dynamic observations of heavy-ion damage in Fe and Fe–Cr alloys, J. Nucl. Mater. 389 (2) (2009) 197–202.
[69] B. Masters, Dislocation loops in irradiated iron, Nature 200 (4903) (1963), 254–254.
[70] Z. Yao, M. Jenkins, M. Hernández-Mayoral, M. Kirk, The temperature dependence of heavy-ion damage in iron: a microstructural transition at elevated temperatures, Phil. Mag. 90 (35–36) (2010) 4623–4634.
[71] S. Dudarev, R. Bullough, P. Derlet, Effect of the $\alpha-\gamma$ phase transition on the stability of dislocation loops in bcc iron, Phys. Rev. Lett. 100 (13) (2008) 135503.
[72] A. Calder, D.J. Bacon, A. Barashev, Y.N. Osetsky, Effect of mass of the primary knock-on atom on displacement cascade debris in α-iron, Phil. Mag. Lett. 88 (1) (2008) 43–53.
[73] J. Marian, B.D. Wirth, J.M. Perlado, Mechanism of formation and growth of<100> interstitial loops in ferritic materials, Phys. Rev. Lett. 88 (25) (2002) 255507.
[74] K. Arakawa, T. Amino, H. Mori, Direct observation of the coalescence process between nanoscale dislocation loops with different Burgers vectors, Acta Mater. 59 (1) (2011) 141–145.
[75] K. Arakawa, M. Hatanaka, E. Kuramoto, K. Ono, H. Mori, Changes in the Burgers vector of perfect dislocation loops without contact with the external dislocations, Phys. Rev. Let. 96 (12) (2006) 125506.
[76] B. Eyre, R. Bullough, On the formation of interstitial loops in bcc metals, Phil. Mag. 12 (115) (1965) 31–39.
[77] M. Li, M. Kirk, P. Baldo, D. Xu, B. Wirth, Study of defect evolution by TEM with in situ ion irradiation and coordinated modeling, Phil. Mag. 92 (16) (2012) 2048–2078.
[78] A. Debelle, M. Barthe, T. Sauvage, First temperature stage evolution of irradiation-induced defects in tungsten studied by positron annihilation spectroscopy, J. Nucl. Mater. 376 (2) (2008) 216–221.
[79] P.M. Derlet, BCC Metals in Extreme Environments: Modelling the Structure and Evolution of Defects, University of Oxford, 2010.
[80] K.D. Hammond, F. Ferroni, B.D. Wirth, Simulation of helium behavior near subsurface prismatic dislocation loops in tungsten, Fusion Sci. Technol. 71 (1) (2017).
[81] C.M. Barr, G.A. Vetterick, K.A. Unocic, K. Hattar, X.-M. Bai, M.L. Taheri, Anisotropic radiation-induced segregation in 316L austenitic stainless steel with grain boundary character, Acta Mater. 67 (2014) 145–155.
[82] R. Valiev, Nanostructuring of metals by severe plastic deformation for advanced properties, Nat. Mater. 3 (8) (2004) 511.
[83] G.A. Vetterick, J. Gruber, P.K. Suri, J.K. Baldwin, M.A. Kirk, P. Baldo, Y.Q. Wang, A. Misra, G.J. Tucker, M.L. Taheri, Achieving radiation tolerance through non-equilibrium grain boundary structures, Sci. Rep. 7 (1) (2017), 12275.
[84] M. Samaras, P. Derlet, H. Van Swygenhoven, M. Victoria, Computer simulation of displacement cascades in nanocrystalline Ni, Phys. Rev. Lett. 88 (12) (2002), 125505.
[85] G.S. Was, Fundamentals of Radiation Materials Science: Metals and Alloys, Springer, 2016.
[86] M. Wen, N.M. Ghoniem, B.N. Singh, Dislocation decoration and raft formation in irradiated materials, Phil. Mag. 85 (22) (2005) 2561–2580.
[87] O. El-Atwani, E. Esquivel, M. Efe, Y. Wang, S.A. Maloy, Detailed transmission electron microscopy study on the mechanism of dislocation loop rafting in tungsten, Acta Mater. 147 (2018) 277–283.
[88] F. Zoepfl, V. Markovic, J. Silverman, Differential scanning calorimetry studies of irradiated polyethylene: I. Melting temperatures and fusion endotherms, J. Polym. Sci. A Polym. Chem. 22 (9) (1984) 2017–2032.
[89] R. Barnes, D. Mazey, Stress-generated prismatic dislocation loops in quenched copper, Acta Metall. 11 (4) (1963) 281–286.
[90] S.J. Zinkle, B.N. Singh, Microstructure of neutron-irradiated iron before and after tensile deformation, J. Nucl. Mater. 351 (1) (2006) 269–284.
[91] R.W. Balluffi, Vacancy defect mobilities and binding energies obtained from annealing studies, J. Nucl. Mater. 69 (1978) 240–263.
[92] M. Griffiths, M. Loretto, R. Smallman, Electron damage in zirconium: I. defect structure and loop character, J. Nucl. Mater. 115 (2–3) (1983) 313–322.
[93] D. Mason, X. Yi, M. Kirk, S. Dudarev, Elastic trapping of dislocation loops in cascades in ion-irradiated tungsten foils, J. Phys. Condens. Matter 26 (37) (2014), 375701.
[94] M. Gilbert, S. Dudarev, P. Derlet, D. Pettifor, Structure and metastability of mesoscopic vacancy and interstitial loop defects in iron and tungsten, J. Phys. Condens. Matter 20 (34) (2008) 345214.
[95] S. Zinkle, Microstructure of ion irradiated ceramic insulators, Nucl. Instrum. Methods Phys. Res. Sect. B Beam Interact. Mater. Atoms 91 (1–4) (1994) 234–246.
[96] F. Ferroni, E. Tarleton, S. Fitzgerald, Dislocation dynamics modelling of radiation damage in thin films, Model. Simulat. Mater. Sci. Eng. 22 (4) (2014) 045009.